RSC Advances

PAPER

View Article Online
View Journal | View Issue

Cite this: *RSC Adv.*, 2019, **9**, 25358

Structure properties and dielectric relaxation of $Ca_{0.1}Na_{0.9}Ti_{0.1}Nb_{0.9}O_3$ ceramic

Hanen Ghoudi,*[a] Souad Chkoundali,[b] Zeineb Raddaoui[c] and Abdelhedi Aydi[b]

In this paper, the synthesis of $Ca_{0.1}Na_{0.9}Ti_{0.1}Nb_{0.9}O_3$ (CNTN) ceramic by a solid-state reaction method is reported. The results of Rietveld refinement of X-ray diffraction (XRD) patterns at room temperature showed a pure tetragonal perovskite (*P4mm* space group). Raman spectroscopy analysis, ranging from of 50 to 1000 cm^{-1}, at room temperature, validates the results of XRD. The dielectric properties was studied by complex impedance spectroscopy examined in broad frequency range, 100 Hz to 200 kHz, at different temperatures. The dielectric permittivity for our CNTN compound confirms the typical relaxor behavior. The investigation of the diffuseness of the transition was conducted by fitting the experimental data with modified Curie–Weiss law; Gaussian distribution and Power law confirm the presence of a short-range association between the polar nanoregions (PNRs). The obtained values of the diffuseness coefficient are of the order 1.6, which corresponds to the diffuse phase transition (DPT) ascribed to the existence of various states of polarization, thus various relaxation times in different regions. The value of diffuseness is of the order 85 and the degree of relaxor (ΔT_{cm} = 65 K) is interesting as far as microelectric applications are concerned. Moreover, based on the frequency dependence of temperature at dielectric maxima using Vogel–Fulcher relationship, a strong evidence for a static freezing temperature with regards to thermally-activated polarization fluctuations was found.

Received 26th May 2019
Accepted 5th August 2019

DOI: 10.1039/c9ra03967h

rsc.li/rsc-advances

1. Introduction

Oxide materials with perovskite structure, having a general formula ABO_3, represent the backbone of the ferroelectric industry. For a long time, ferroelectric ceramics have proved to be useful for various practical applications, such as high dielectric constant capacitors, radio and communication filters, pyroelectric devices, medical diagnostic transducers, ultrasonic motors and electro-optic light valves.[1–5] The relaxor ferroelectrics are a class of disordered crystals with peculiar structure and properties.[6] The typical dielectric response, for example, has a frequency and temperature dependent diffuse permittivity maximum. However, most of relaxor compounds are complex lead-based perovskites, namely $Pb(Mg_{1/3}Nb_{2/3})O_3$ (PMN)[7] or (Pb, La)·(Zr, Ti)O_3 (PLZT).[8] In recent years, materials with lead-free compositions have attracted much interest for environment-friendly applications. Promising compounds are $BaTiO_3$ based solid solutions, such as Ba(Ti, Sn)O_3,[9,10] Ba(Ti, Zr)O_3,[11] $Ba_{0.8}Sr_{0.2}TiO_3$ [12,13] or $BiFeO_3$.[14]

Thanks to its numerous electric, dielectric and optical properties, calcium titanate ($CaTiO_3$) has been widely investigated.[15,16] $CaTiO_3$ with orthorhombic distortions of the perovskite structure was observed from X-ray diffraction by Naray-Szabo.[17] It is characterized by paraelectric property at room temperature, dielectric permittivity above 170 and a dissipation factor (D) $\sim 10^{-3}$ at 1 kHz.[18] Lemanov *et al.*[19] measured the dielectric properties of $CaTiO_3$. They classified this perovskite as a ferroelectric at temperature below 300 K (ε_r = 330 at 4.2 K).

At room temperature, pure $NaNbO_3$ is an antiferroelectric with an orthorhombic distorted perovskite along with a *Pbma* space group.[20] This compound undergoes several phase transitions. The dielectric behavior of $NaNbO_3$ sample has been widely examined. It displays a phase transition at T_C around 913 K with a maxima real permittivity of ε'_{rmax} 1750 at T_C.[21]. Recently, several authors have reported that $NaNbO_3$ becomes ferroelectric with similar behavior related to $KNbO_3$,[22] $LiNbO_3$.[23]

$NaNbO_3$ substituted $CaTiO_3$ reveals suppression of quantum fluctuations, when the concentration of $NaNbO_3$ exceeds 2%.[24] SSNNx is a solid solution based on a mixture of $NaNbO_3$ and $SrSnO_3$. It is considered as an advanced ferroelectric ceramic for environment-friendly applications.[25]

In the mixed system 1–$x$$NaNbO_3$–$x$$CaTiO_3$, the dielectric permittivity shows a morphotropic phase boundary ceramics. The well known MPB is nonferroelectric and nonpiezoelectric at room temperature.[26]

[a]*Laboratoire de physique des Matériaux et des Nanomatériaux Appliquée à l'environnement, Faculté des Sciences de Gabès, Université de Gabès, Tunisia. E-mail: hanengoudi2@gmail.com*

[b]*Laboratoire des Matériaux Multifonctionnels et Applications, Faculté des Sciences de Sfax (FSS), Université de Sfax, B. P.1171, 3018 Sfax, Tunisia*

[c]*Laboratoire de la Matière Condensée et des Nanosciences, Faculté des Sciences de Monastir, Université de Monastir, Tunisia*

This study was undertaken to study the behavior of the relaxors, the structural and dielectric properties of the mixed oxide system $CaTiO_3$–$NaNbO_3$ (CT–NN). This work is also intended to explore the effects of substitutions in sites A and B on their structural, dielectric and Raman properties. In this regard, the $NaNbO_3$ solid solution was selected as the antiferroelectric material and $CaTiO_3$ was added to investigate the relaxor behavior in a lead-free sample.

Considered as environment-friendly materials, these lead-free compounds could be highly significant regarding the scope of application.

2. Experimental procedure

2.1. Sample preparation

The polycrystalline sample of CNTN was prepared by solid-state reaction using the oxides $CaCO_3$, Na_2CO_3, Nb_2O_3 and TiO_2, Aldrich with 99.9 of purity, in suitable stoichiometries. The stoichiometrically weighed composition was thoroughly mixed in an agate for 1 h. The powder was then pressed into discs and calcinated at 1373 K for 12 h, to obtain a single phase sample. After calcination, the powder was mixed for 1 h and one part of it was pressed under 100 MPa into discs of an 8 mm diameter and about a 1 mm thickness. Ultimately, the formed pellets were sintered at 1523 K for 3 h with a speed of 200 °C h^{-1}, in an oxygen-rich atmosphere.

The microstructure was analyzed using scanning electron microscopy (SEM). The pictures were taken at room temperature (with 15 kV) on a JEOL JED 2300.

The identification of phase purity, homogeneity and crystallinity of polycrystalline sample was performed *via* powder X-ray diffraction (XRD) analysis, at room temperature, by means of an XPERT-PRO diffractmeter with a graphite monochromatized CuK_α radiation (λCuK_α = 1.54 Å). The data collected in the range of $19 \leq 2\theta \leq 109$ with a step-size of 0.02° and a counting time of 10 s per step were analyzed by the Fullprof software based on the Rietveld method[27].

The Raman spectroscopy was recorded in the frequency range 70–1000 cm^{-1}, in a micro-Raman Spectrometer LABRAM HR800. The excitation source was the 633 nm lines of He^+ ion laser, working in a back scattering. The spectral resolution of the system was 3 cm^{-1}. The deconvoluted Raman active modes for CNTN were determined by fitting with a combined pseudo-Voigt using the LabSpec5 software.

The weight and geometrical dimensions of the cylindrical pellets (m_p = 0.2, e = 1 mm) are the main characteristics, determining the experimental density $\left(d_{exp} = \frac{m_p}{\pi(\phi/2)^2 e}\right)$, which was compared to the theoretical density ($d_{theor} = \frac{Z \times M}{N_A \times V}$ where ($Z = 1$) stands for the number of atoms, $N_A = 6.02 \times 10^{23}$ represents the Avogadro's number, M denotes the molecular weight and V is the volume of tetragonal unit cell) determined from X-ray measurements. Hence, the compactness was calculated as the ratio $C = \frac{d_{exp}}{d_{theor}}$ Table 1 shows the values of ρ_{theo}, ρ_{exp} and C. According to this table, CNTN compound is characterized by an excellent quality.

To acquire dielectric measurements, gold electrodes were sputtered on the circular faces of the ceramic discs. The measurement of the real parts pertaining to the relative dielectric permittivity (ε'_r) was carried out *via* a Wayne–Kerr 6425 impedance analyser (from 100 Hz to 200 kHz), in the temperature range of 82 K to 500 K, with a heating rate of 2 K min^{-1}.

3. Results and discussions

3.1. Morphological and X-ray diffraction analysis

Fig. 1 shows the SEM micrographs of the CNTN ceramic and the inset represents the grains size distribution histograms. The SEM image reveals that this compound has a homogenous microstructure and well-developed grains. The mean particle size of the sample was estimated by using ImageJ software. After measuring the diameters of the particle in SEM image, the obtained data were fitted with the lognormal function.

$$f(D) = \left(\frac{1}{\sqrt{2\pi\sigma D}}\right)\exp\left[-\frac{\ln^2\left(\frac{D}{D_0}\right)}{2\sigma^2}\right] \quad (1)$$

where D_0 and σ are the median diameter obtained from the SEM and data dispersions, respectively, for CNTN compound. The inset of Fig. 1 exhibits the grains size distribution for CNTN compound. The mean diameter $\langle D\rangle = D_0 \exp(\sigma^2/2)$ and $\sigma_D = \langle D\rangle [\exp(\sigma^2) - 1]^{1/2}$ standard deviation were determined using fit results (Table 2). The mean diameter of CNTN sample is 0.51 μm.

Fig. 2 shows the X-ray diffraction patterns for the CNTN sample taken at room temperature. This figure displays the formation of a single phase sample without any detectable impurities at least in the sensitivity range of our

Table 1 The crystal data and refinement factors obtained by the Rietveld refinement of XRD patterns for $Ca_{0.1}Na_{0.9}Ti_{0.1}Nb_{0.9}O_3$

$Ca_{0.1}Na_{0.9}Ti_{0.1}Nb_{0.9}O_3$		
Density theo	Theo (g cm^{-3})	5.39
Density (exp)	Exp (g cm^{-3})	5.12
Compactness	C	95%
Space group	*P4mm*	
Cell parameters	$a = b$ (Å)	3.925(1)
	c (Å)	4.012(4)
	c/a	1.022(2)
	V (Å^3)	61.807(2)
Thermal agitation	(Na/Ca) Biso (Å^2)	1.133(3)
	(Nb/Ti) Biso (Å^2)	0.201(0)
	(O_1) Biso (Å^2)	1.000(0)
	(O_2) Biso (Å^2)	1.022(0)
Bond lengths and bond angles	$\langle d_{(Nb/Ti-O)}\rangle$	1.917
	$\langle \theta_{(Nb/Ti-O-Nb/Ti)}\rangle$	138.59
Agreement factors	R_p (%)	10.2
	R_{wp}	16.2
	χ^2	3.54

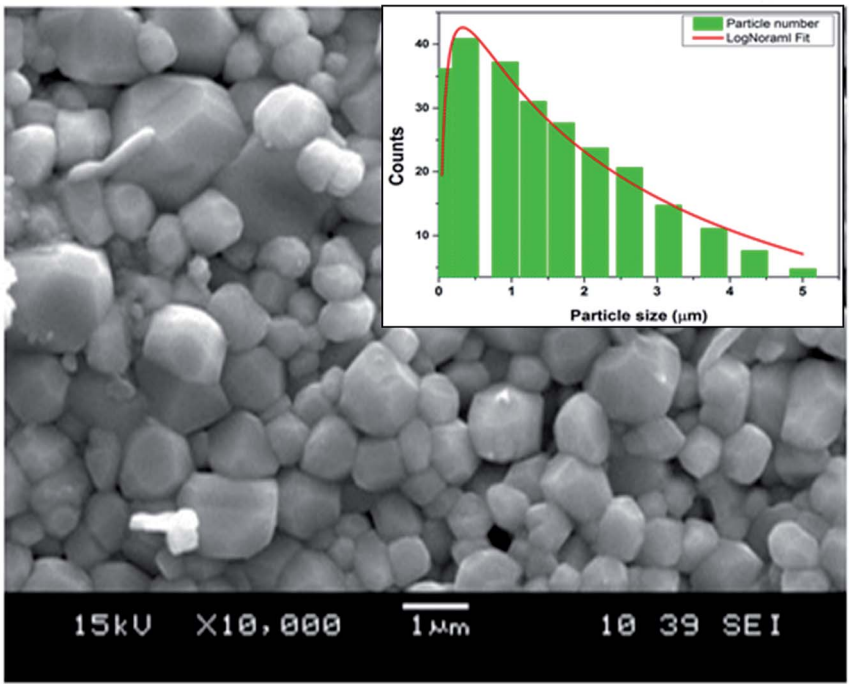

Fig. 1 SEM image of the sample $Ca_{0.1}Na_{0.9}Ti_{0.1}Nb_{0.9}O_3$ ceramic. The inset shows the size distribution histogram.

experimental apparatus, which indicates that Ca^{2+} and Ti^{4+} diffused into $NaNbO_3$ lattices to form a new composition, CNTN. We found a good agreement between the observed and calculated profiles. The diffraction peaks were indexed in the tetragonal structure with the *P4mm* space group, with (Na/Ca): 1a (0, 0, 0), (Nb/Ti): 1b (0.5, 0.5, *z*), O1: 1b (0.5, 0.5, *z*) and O2: 2c (0.5, 0, *z*). Through the Rietveld refinement analysis, we estimated the lattice parameters, unit cell volume and fitting parameters were estimated. In fact, Table 1 represents the detailed results of Rietveld refinements. It can be noted that the partial replacement of Na^+ by Ca^{2+} in site A and Ti^{4+} by Nb^{5+} in site B confirms the regular deviation of Nb/Ti–O–Nb/Ti bond angles and the Ti–O bond length (Table 1). However, the value of distance and angle data with the effect of the substitution indicates that the TiO_6 octahedral framework has a slight distortion (inset of Fig. 2).

These observations are consistent with the crystal structure and the TiO_6 octahedron for the CNTN sample determined using "Diamond" program which, based on the refined atomic positions find by XRD, was represented graphically as illustrated in the inset of Fig. 2(b). From this figure, the lattice distortion in our compound can be observed.

Table 2 Calculated grain sizes, crystallite sizes and strains of $Ca_{0.1}Na_{0.9}Ti_{0.1}Nb_{0.9}O_3$

Sample	D_{Sch} (nm)	D_{W-H} (nm)	D_{SEM} (μm)	Strain (ε)
$Ca_{0.1}Na_{0.9}Ti_{0.1}Nb_{0.9}O_3$	150	160	0.51	0.0580

To validate the experimental observations, the results were compared with the Goldschmidt tolerance factor *t*,[28] expressed by:

$$t = \frac{(0.1r_{Ca^{2+}} + 0.9r_{Na^+}) + r_{O^{2-}}}{\sqrt{2}((0.1r_{Ti^{4+}} + 0.9r_{Nb^{5+}}) + r_{O^{2-}})} \quad (2)$$

where $r_{Na^+} = 1.39$ Å, $r_{Ca^{2+}} = 1.34$ Å, in a twelvefold coordination; $r_{Nb^{5+}} = 0.64$ Å, $r_{Ti^{4+}} = 0.6$ Å in a sixfold coordination and $r_{O^{2-}} = 1.35$ Å.[29]

Based on the values of the ionic radii of the various atoms, we estimated the tolerance factor value ($t = 0.97$), ranging in a stable pervoskite structure. This result is in line with the results of the refinement.

The average crystallite size of our CNTN compound was estimated using different methods, such as Scherrer formula (Sch) and Williamson–Hall formula (W–H).

Scherrer formula is as follows:[30]

$$D_{Sch} = \frac{K\lambda}{\beta \cos\theta} \quad (3)$$

where K is a constant equal to 0.9, β is the breadth of the detected diffraction line at its half intensity maximum on the highest peak of plane (313), λ is the used X-ray wavelength and θ is the Bragg angle of the most intense peak. The instrumental broadening factor[31] was considered during the FWHM calculation $\left(\beta = \sqrt{{\beta_{exp}}^2 - {\beta_{inst}}^2}\right)$. The values of D_{Sch} are given in Table 2.

Depending on different θ positions, the separation of size and strain broadening analysis was based on Williamson–Hall

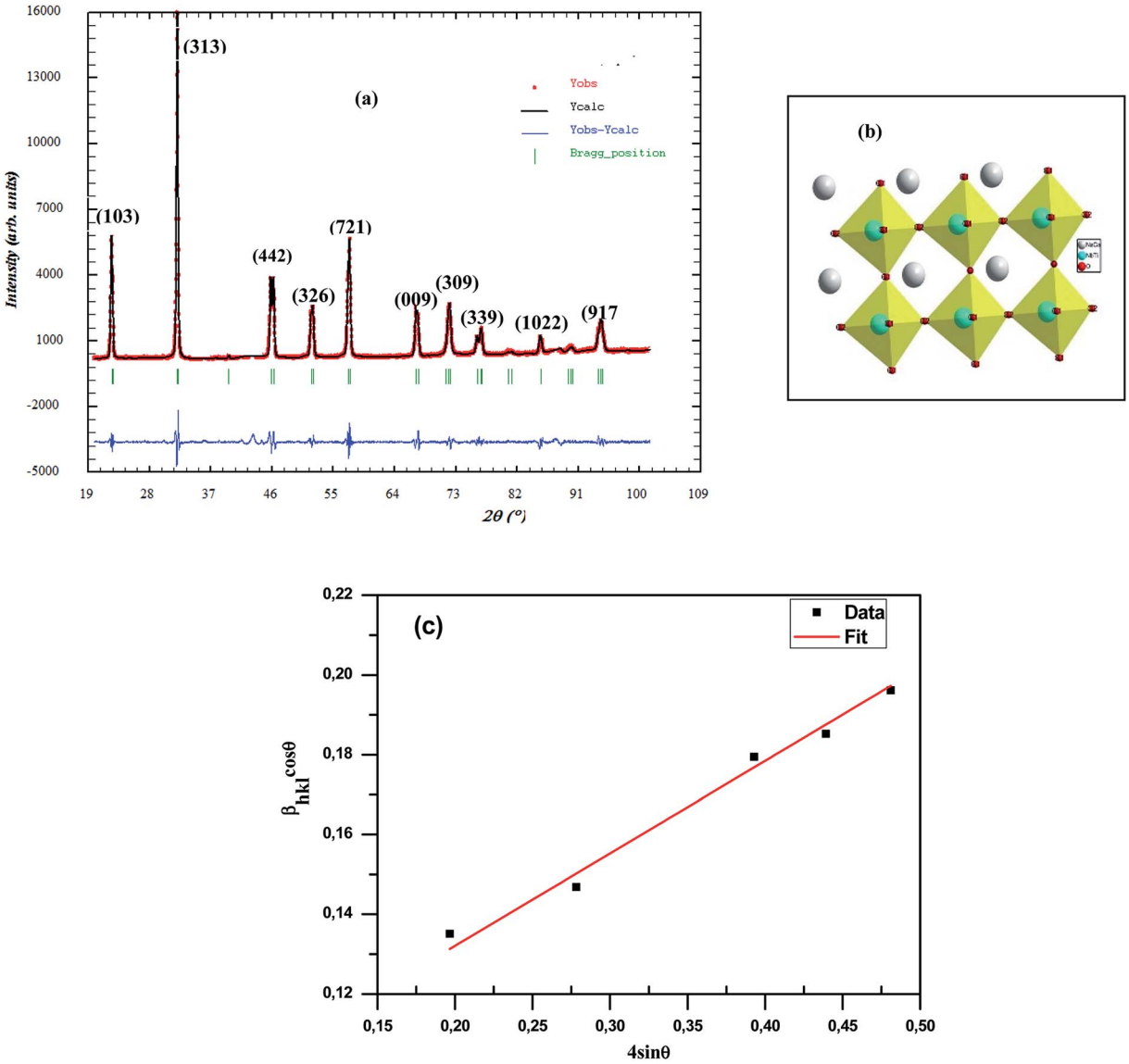

Fig. 2 (a) Rietveld plots of XRD data for polycrystalline $Ca_{0.1}Na_{0.9}Ti_{0.1}Nb_{0.9}O_3$ ceramic, (b) the crystal structure for the sample $Ca_{0.1}Na_{0.9}Ti_{0.1}Nb_{0.9}O_3$ ceramic and the distortion of TiO_6, (c) strain graph of the tetragonal phase of $Ca_{0.1}Na_{0.9}Ti_{0.1}Nb_{0.9}O_3$.

(W–H) method.[32] The calculation of strain contribution is given by:

$$\varepsilon = \frac{\beta}{4 \tan \theta} \quad (4)$$

Line broadening evidently combines crystallite size and strain, as represented by the following equation:

$$\beta = \frac{K\lambda}{D_{W-H} \cos \theta} + 4\varepsilon \tan \theta \quad (5)$$

In a more simplified way:

$$\beta \cos \theta = \frac{K\lambda}{D_{W-H}} + 4\varepsilon \sin \theta \quad (6)$$

The value of ε is calculated based on the slope of $\beta \cos \theta$ *vs.* $4 \sin \theta$ plot.

This gives an equation of a straight line between $\beta \cos \theta$ and $4 \sin \theta$. Plotting $\beta \cos \theta$ (y-axis) and $4 \sin \theta$ (x-axis), the slope of the line yields the strain (ε) and the crystallite size (D) can be calculated from the intercept $\left(= \frac{\lambda k}{D_{W-H}}\right)$ of this line on the y-axis, Fig. 2(c). Indeed, Table 2 illustrates the calculated values pertaining to the structural parameters.

From these calculations, we found that the average crystallite size calculated in the present system using W–H method (D_{W-H}) is larger than that from Scherrer method (D_{Sch}) because the broadening effect due to strain is completely excluded in Scherrer method.[33] In addition, we notice that the grains detected by SEM are obviously much larger compared to those

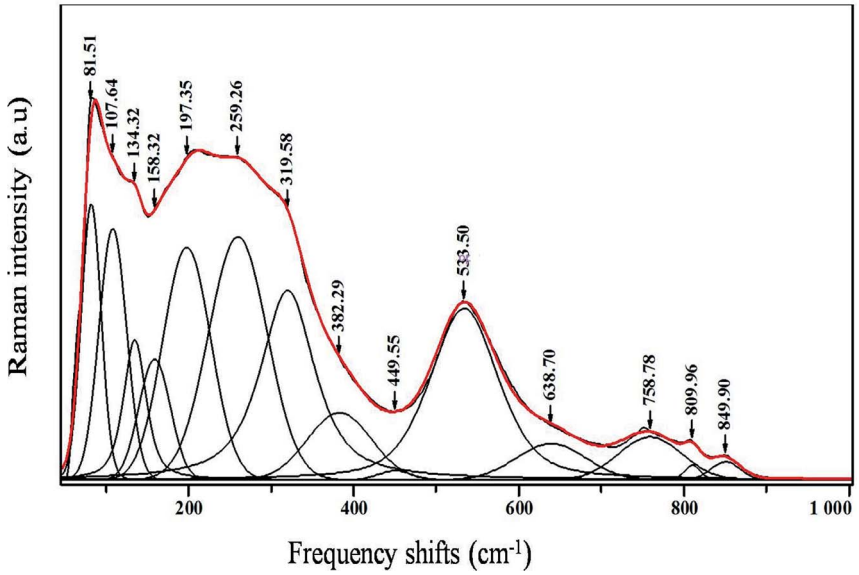

Fig. 3 Raman spectra of $Ca_{0.1}Na_{0.9}Ti_{0.1}Nb_{0.9}O_3$ at room temperature.

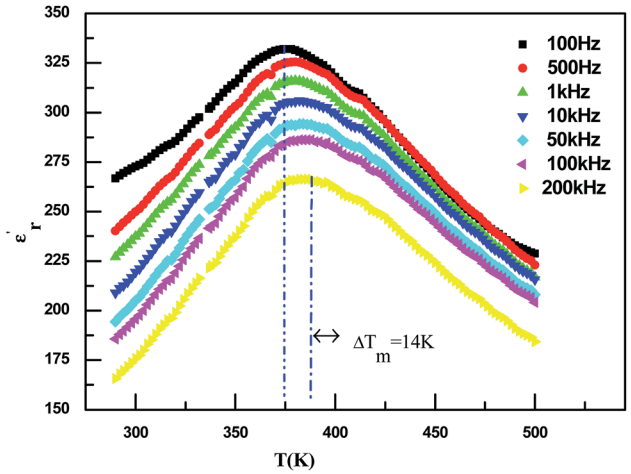

Fig. 4 Temperature dependence on the permittivity ε'_r at various frequencies of $Ca_{0.1}Na_{0.9}Ti_{0.1}Nb_{0.9}O_3$ ceramic.

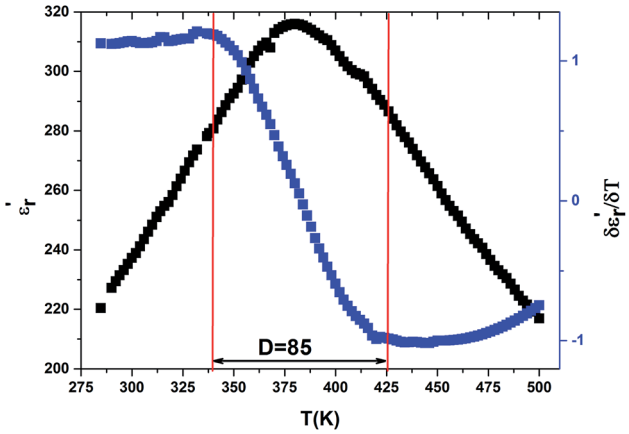

Fig. 5 The variation of $\partial\varepsilon'_r/\partial T$ and the value of the diffuseness degree for $Ca_{0.1}Na_{0.9}Ti_{0.1}Nb_{0.9}O_3$ ceramic.

calculated by XRD. Therefore, this indicates that each grain detected by SEM is composed of several crystallized grains.[34]

3.2. Raman spectroscopy

Raman spectroscopy was carried out for the sample in order to further study the changes in the crystal structure and the presence of functional groups, also to correlate our structural information with the Raman data that we obtained.

Table 3 Physical properties of $Ca_{0.1}Na_{0.9}Ti_{0.1}Nb_{0.9}O_3$ ceramic

$\Delta\varepsilon'_r/\varepsilon'_r$	C (K) $\times 10^5$	T_0 (K)	T_m (K)	T_{dev} (K)	ΔT_{cm} (K)	ΔT_m (K)	D
0.154	1.544	340	378	443	65	14	85

The room temperature deconvolution of Raman spectrum of CNTN ceramic is shown in Fig. 7. The spectra are similar to that of $NaNbO_3$ in tetragonal phase.[35] The Raman spectrum of the tetragonal CNTN showed 14 vibration modes. These results, accordingly, are in line with the ones proposed by S. D. Ross,[36] Juang[37] and L. B. Abdessalem *et al.*[38] In our compound, the peaks detected at 81, 107, 134 and 158 cm^{-1} were attributed to the Na–O bonds of the A-site vibration in the perovskite with an ABO_3 general formula.[39,40] Modes observed at 638.70 cm^{-1} are dominated by vibrations, involving chiefly oxygen displacements. The oxygen vacancies are present by the two latest modes (*i.e.*, at 809 and 849 cm^{-1}),[40,41] which can be described as:

$$Nb \xrightarrow{Ti} Nb'_{Ti} + V^{\cdot}_{O} \quad (7)$$

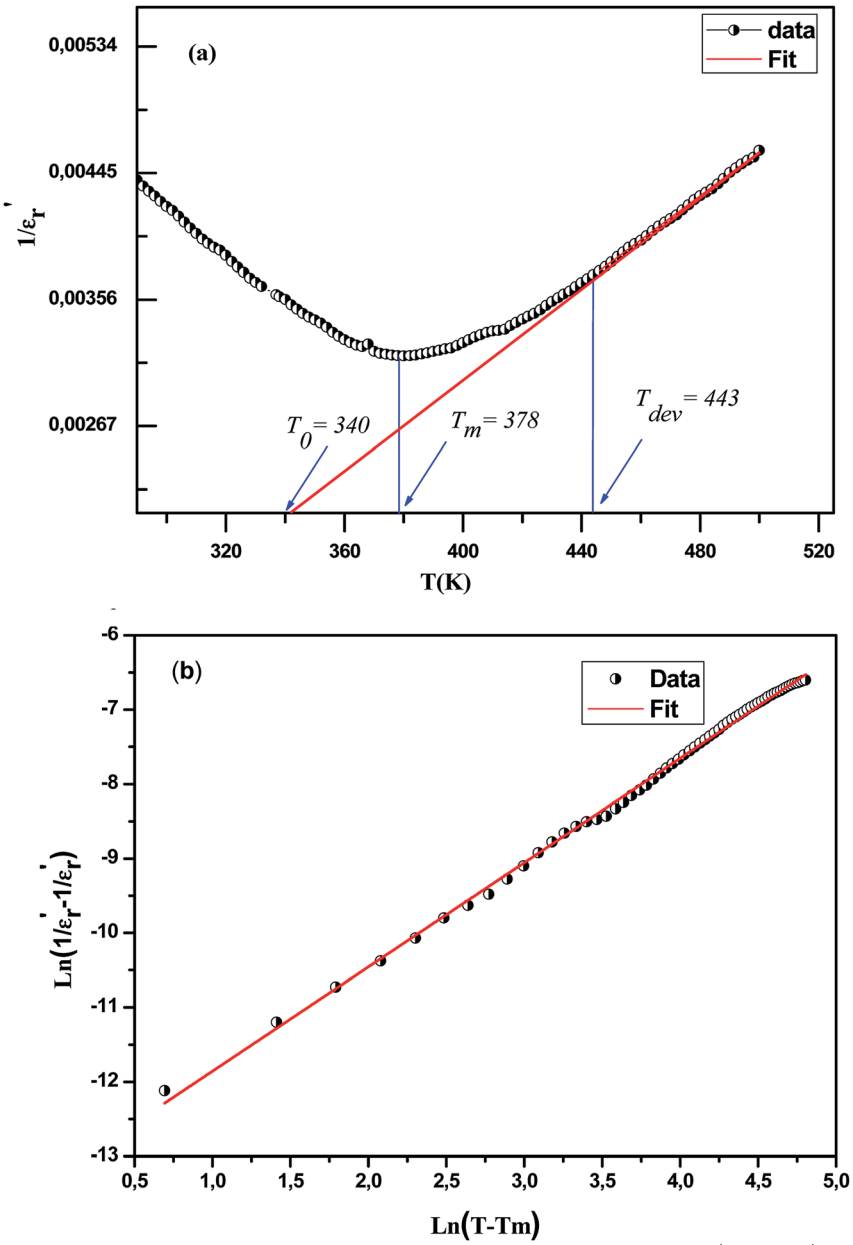

Fig. 6 The variation of $\frac{1}{\varepsilon'_r}$ *versus* temperature for $Ca_{0.1}Na_{0.9}Ti_{0.1}Nb_{0.9}O_3$ ceramic (a); the variation of $\ln\left(\frac{1}{\varepsilon'_r} - \frac{1}{\varepsilon'_{rmax}}\right)$ as a function of $\ln(T - T_m)$ at 100 kHz for this compound (b).

The bands around 259 and 533 cm^{-1} are assigned to the mode of A_1 (TO) symmetry. However, the bands around 319; 382 and 449 cm^{-1}, signaling out the tetragonal phase, are ascribed to the E (TO + LO) + B_1 mode.[42] The A_1 (LO) modes can be detected at 809 and 849 cm^{-1}. The peaks assigned to the Nb–O phonon Raman spectrum are identified at 276 cm^{-1} for $NaNbO_3$.[43–45]. On the other hand, in the CNNT, they are observed at 259 cm^{-1} (Fig. 3). This behavior means that the substitution of $NaNbO_3$ by Ca^{2+} in A site and by Ti^{4+} in B site of the perovskite structure gives rise to an important disorder in the structure. These results are in compliance with the results related to the XRD (Fig. 2(a)) patterns from the variation of *c*/*a* ratio and the volumes of cell parameter of our compound (Table 1).

This structural distortion and slight change in the local symmetry of the CNTN sample can affect the dielectric property by confirming the relaxor behavior for this sample.

3.3. Dielectric studies

The evolution of the real part of the permittivity as a function of the temperature and the frequency of the CNTN ceramic is shown in Fig. 4. The studied system exhibits the distinctive feature of relaxor ferroelectrics, namely a strong dispersion of the maximum of ε'_{rmax} at $T < T_m$ (T_m is the maximum permittivity temperature) which shifts towards higher temperature by decreasing progressively the value of ε'_r as the frequency increases. The relaxor phenomenon has recently been explored

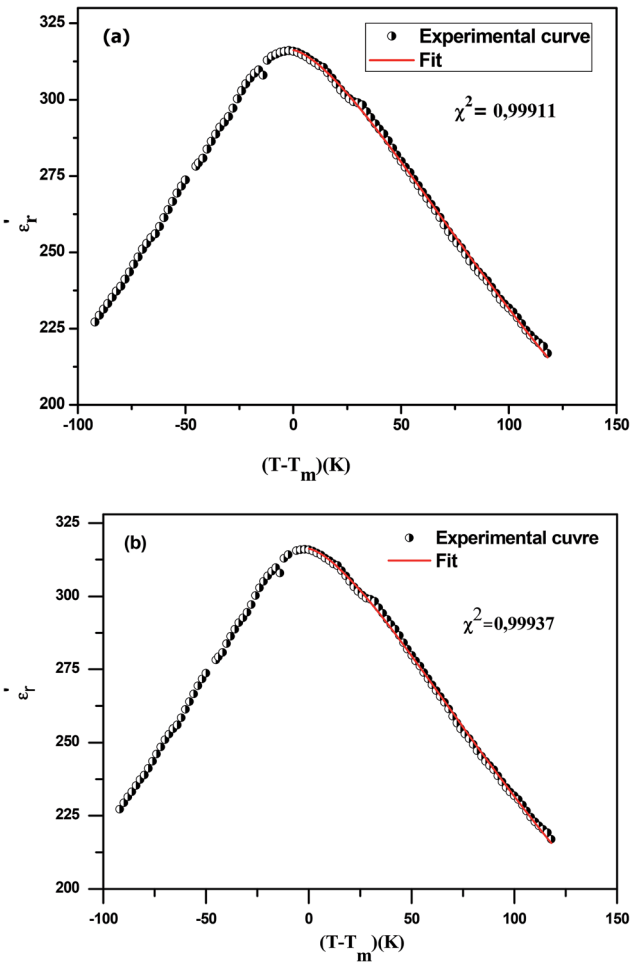

Fig. 7 The experimental and fitted dielectric data *versus* temperature for $Na_{0.9}Ca_{0.1}Nb_{0.9}Ti_{0.1}O_3$ ceramic using eqn (11) (a) and (12) (b).

in perovskite structure, *viz.* $Ba_{1-x}Na_x(Ti_{0.8}Sn_{0.2})_{1-x}NbO_3$,[46] $(Pb_{1-3x/2}La_x)(Mg_{1/3}Nb_{2/3})O_3$,[47] $0.3Bi_{1-x}Y_xFeO_3$-$0.7Ba_{0.8}Sr_{0.2}TiO_3$ (ref. 48) and $(Pb_{1-3x/2}La_x)(Zr_{1-y}Ti_y)O_3$.[49] The diffuse dielectric behavior of relaxor materials has been attributed to the compositional fluctuation (*i.e.*, the presence of a microscopic domain in the macro polar region) and to the structural disorder in crystallographic sites when one or more cations occupy the same site in the structure;[50–53] in our case Ca^{2+} by Na^+ in site A and Ti^{4+} by Nb^{5+} in site B. Table 3 shows the relaxor characteristics for our composition as the T_m shift, $\Delta T_m = (T_m\ (2 \times 10^5\ \text{Hz}) - T_m\ (10^2\ \text{Hz}))$, and the relative dispersion $\frac{\Delta\varepsilon_r'}{\varepsilon_r'} = \frac{(\varepsilon_r'(10^2\ \text{Hz}) - \varepsilon_r'(2 \times 10^5\ \text{Hz}))}{\varepsilon_r'(2 \times 10^5\ \text{Hz})}$.

The width of the transition represents the DPT for the CNTN compound, which is very important in ferroelectric materials. We can define '*D*' as the distinctive parameter of diffuseness degree. This is defined as:[54]

$$D = T_{\left(\frac{\partial\varepsilon_r'(T)}{\partial T}\right)_{min}} - T_{\left(\frac{\partial\varepsilon_r'(T)}{\partial T}\right)_{max}} \quad (8)$$

where $T_{\left(\frac{\partial\varepsilon_r'(T)}{\partial T}\right)_{min}}$ and $T_{\left(\frac{\partial\varepsilon_r'(T)}{\partial T}\right)_{max}}$ are the temperature when $\left[\frac{\partial\varepsilon_r'(T)}{\partial T}\right]$ reaches the minimum and maximum, respectively. The curves for the $\left[\frac{\partial\varepsilon(T)}{\partial T}\right]$ against (T) for the sample are indicated in Fig. 5. The temperature interval between $T_{\left(\frac{\partial\varepsilon(T)}{\partial T}\right)_{min}}$ and $T_{\left(\frac{\partial\varepsilon(T)}{\partial T}\right)_{max}}$ reflects the diffuseness degree microscopically. The vertical dashed lines in Fig. 5 correspond to $T_{\left(\frac{\partial\varepsilon(T)}{\partial T}\right)_{min}}$ and $T_{\left(\frac{\partial\varepsilon(T)}{\partial T}\right)_{max}}$ values. The interval between them is *D* as indicated.

The value of diffuseness is of the order $D = 85$ (Table 3). Therefore, the phase transition from paraelectric-ferroelectric (T_c) is the transition that is more diffuse.

With reference to the T_m transition temperature, the dielectric constant ε_r' and the Curie temperature T_0 of a ferroelectric can be depicted by the Curie–Weiss law as follows:

$$\frac{1}{\varepsilon_r'} = \frac{(T - T_0)}{C}\ (T > T_c) \quad (9)$$

where T_0 stands for the Curie temperature and C the Curie–Weiss constant.

Fig. 6(a) exhibits the inverse of the dielectric constant $\left(\frac{1}{\varepsilon_r'}\right)$ depending on the temperature at 1 kHz. A deviation from Curie–Weiss law is detected in this sample. The parameter ΔT_{cm} refers to the degree of deviation from the Curie–Weiss law and is expressed by: $\Delta T_{cm} = T_{dev} - T_m$ where T_{dev} stands for the temperature at which the dielectric constant starts deviating from Curie–Weiss law and T_m denotes the temperature of the dielectric maximum.

The values of the parameters C, T_0, T_{dev}, T_m and ΔT_{cm} are illustrated in Table 3. ($T_C \neq T_0$) shows that the phase transition is of a first order type.[55] The broadened peaks correspond to the diffuse type transition in this composition, a distinctive feature of a disordered perovskite structure.

To further study the phase transition behavior of the CNTN sample, we calculated the diffuseness parameter using the modified Curie–Weiss law:[56]

$$\frac{1}{\varepsilon_r'} - \frac{1}{\varepsilon_{rmax}'} = \frac{(T - T_m)^\gamma}{C_1} \quad T > T_m \quad (10)$$

The diffuseness coefficient γ allows understanding the character of the phase transition; C_1 is a constant quantity and ε_{rmax}' is the peak dielectric permittivity at temperature T_m. In general, the value of γ between these limits ($1 < \gamma < 2$) provide an incomplete diffuse phase transition. For normal ferroelectrics γ approximate to 1, while relaxor ones approximate to 2.

The inset of Fig. 6(b) shows the plots of $\ln(1/\varepsilon_r' - 1/\varepsilon_{rmax}')$ *versus* $\ln(T - T_m)$ at 1 kHz for CNTN ceramic sample. The obtained values of 'γ' are found in the order of 1.58, which corresponds to the diffuse phase transition assigned to the existence of various states of polarization, thus various relaxation times in different regions.[57] Therefore, the origin of the observed relaxor behavior with DPT in CNTN sample is due to the inhomogeneous distribution assigned to

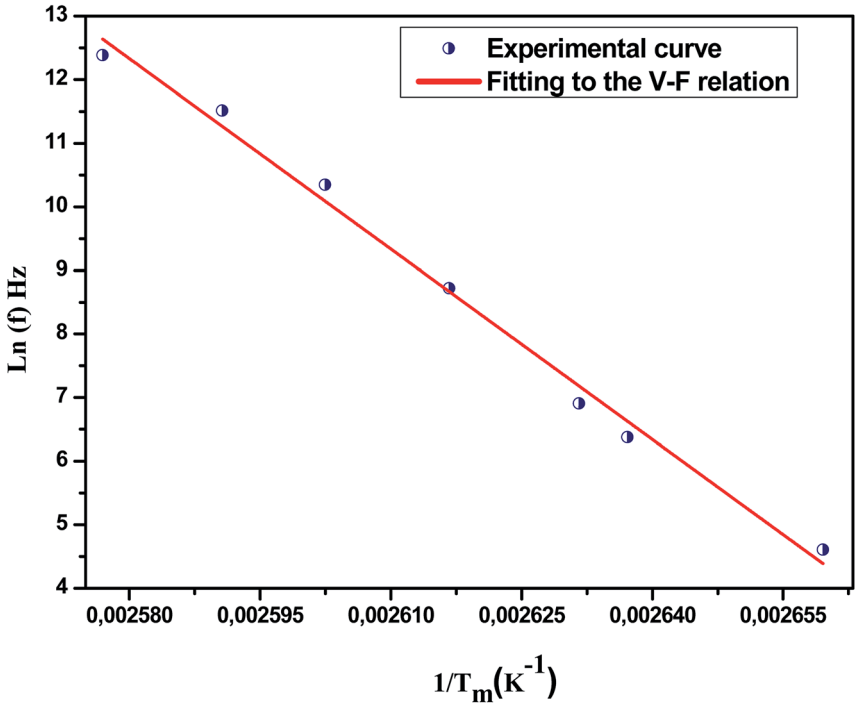

Fig. 8 Fitting of Vogel–Fulcher model to the dielectric relaxation data of $Na_{0.9}Ca_{0.1}Nb_{0.9}Ti_{0.1}O_3$ ceramic.

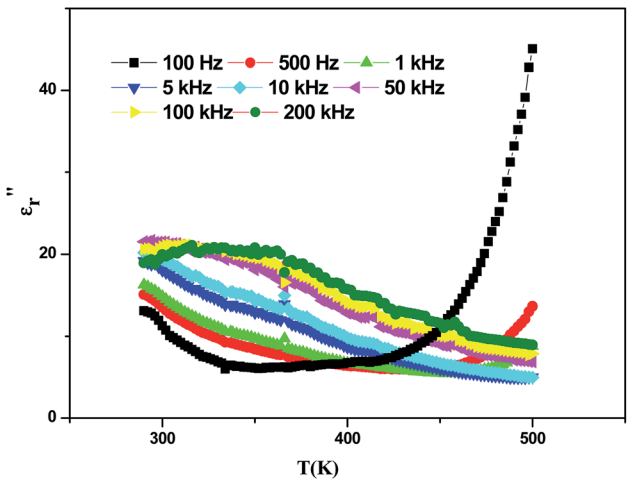

Fig. 9 Thermal variation of the imaginary part of permittivity ε''_r for $Na_{0.9}Ca_{0.1}Nb_{0.9}Ti_{0.1}O_3$ ceramic.

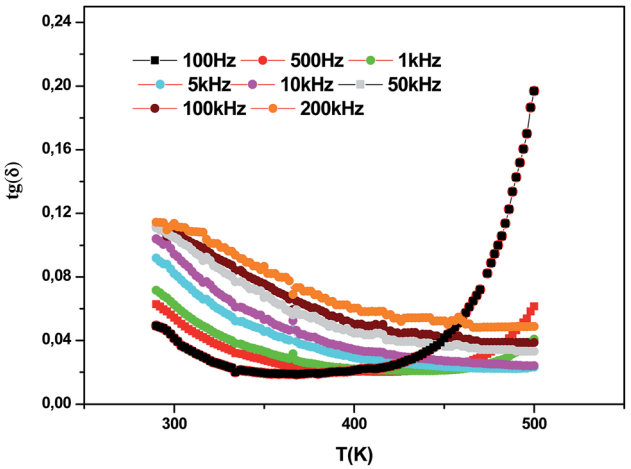

Fig. 10 Thermal variation of the dielectric loss for $Na_{0.9}Ca_{0.1}Nb_{0.9}Ti_{0.1}O_3$.

the compositional fluctuation, resulting in the microscopic heterogeneity with various Curie points and giving rise to the detected behavior Relaxor.[58] Furthermore, the creation of the Coulomb interactions at long distance inhibits the formation of ferroelectric microdomains in favor of the formation of the PNRs. Under these conditions, the order becomes short. Each nanodomain transits at a given temperature, which explains the diffuse character and the widening of the transition, however, no dielectric relaxation at temperatures below T_m. This dielectric dispersion is elucidated by the dynamics of these nanodomains. In fact, this behavior is identical to those mentioned in the literature.[59]

F. Bourguiba and Kirillov *et al.*[60,61] highlight the quadratic relation between the dielectric constant and temperature for ferroelectrics with a diffuse phase transition (relaxor-ferroelectrics). This quadratic law was derived theoretically from a microscopic composition-fluctuation model basis. Assuming that the statistical composition fluctuation in a complex perovskite generates microscopic regions possessing similar dielectric characteristics, but a marginally different Curie temperature, and that the distribution of the Curie temperature is of a Gaussian type as well:[62]

$$\varepsilon'_r = \frac{\varepsilon'_{rm}}{1 + \frac{(T - T_m)^2}{2\delta_1{}^2}} \quad (11)$$

where ε'_{rmax} is the maximum of the real part of the dielectric permittivity, T_m is the temperature of maximum dielectric permittivity and δ_1 is the diffuseness parameter pertaining to the peak broadening of the phase transition.

However, it was found that this Gaussian distribution is not suitable to account for the relaxor behavior in our CNTN compound. Furthermore, the Power law was introduced to explain the dependence of temperature on the dielectric constant and it is given as:[63]

$$\varepsilon'_r = \frac{\varepsilon'_{rm}}{1 + \frac{(T - T_m)^\gamma}{2{\delta_2}^2}} \quad (12)$$

where γ depicts the Curie–Weiss law for $\gamma = 1$ and the total diffuse phase transition for γ tends towards 2. Only when $\gamma = 2$, the parameter δ_2 possesses the dimension of a temperature, revealing, in this case, the temperature extension of the phase transition, *i.e.* the Curie region.

The experimental values are fitted to eqn (11) and (12) and illustrated in Fig. 7(a) and (b). By fitting the experimental data to eqn (12), the value of γ is 1.61, standing for the diffuse phase transition.

Comparing the modified Curie–Weiss law and Power law, it is noted that the values of γ are close.

Overall, the presence of micro-heterogeneities in the perovskite material due to the thermo chemical diffusion controlled by solid-state reactions may account for the relaxor behavior with DPT. In our case, the relaxor behavior is a result of both the substitution of Ca^{2+} by Na^{+} and Ti^{4+} by Nb^{5+} in A and B sites, respectively. Therefore, different states of polarization are caused by such a heterogeneous distribution of cations.

According to the Curie–Weiss law and the value of the empirical parameters such as ΔT_{cm}, γ and ΔT_m, all the characterizations, as determined above, confirmed the relaxor type of the ceramic.

To have a better insight into relaxor ferroelectric character, the maximum dielectric constant (T_m) is found to obey Vogel–Fulcher model.[64] This model observes the interaction between the dipoles, which makes the dipoles freeze at a particular temperature, labeled freezing temperature. Moreover, the relation similar to that recognized for glasses can depict this model,[65] and it is expressed as follows:

$$f = f_0 \exp\left(-\frac{E_a}{k_B(T_m - T_F)}\right) \quad (13)$$

where f_0 is the attempt frequency of dipole reorientation, E_a is a measurement of average activation energy, k_B is the Boltzmann constant and T_F is the freezing temperature. Fig. 8 displays the variation of $\ln f$ (in the range of frequencies 0.1–200 kHz) as a function of $1/T_m$. The experimental curve was fitted using the above mentioned Vogel–Fulcher formula, characterized by the following fitting parameters: $T_F = 137$ K, $E_a = 0.053$ eV and $f_0 = 3.44\ 10^5$ Hz.

In addition, we notice that the pre-exponent factor f_0 elucidates the size of polar clusters and the degree of interaction between them. The smaller the size of the cluster is, the lower the interaction between them is and hence the larger value of f_0 is, and *vice versa*.

Similarly, the low values of the activation energy are also found by H. Ghoudi *et al.*[66] for $(Ba_{0.7}Sr_{0.3})_{1-x}Na_x$ $(Ti_{0.9}Sn_{0.1})_{1-x}Nb_xO_3$ relaxors ($E_a \approx 0.061$ eV). The activation energy E_a, much lower in our ceramic, reflected a lower barrier between two potential wells. This range of features, relating to the potential well, reflected different polarization mechanisms. As shown in this figure (Fig. 8), the model accounts well for the data, suggesting the similarity between the relaxor behavior in the present composition and that of a spin glass model with polarization fluctuations beyond the static freezing temperature.

Fig. 9 and 10 show the thermal evolution of the imaginary part of the permittivity and loss for this $Ca_{0.1}Na_{0.9}Ti_{0.1}Nb_{0.9}O_3$ ceramic. The dielectric losses are about 6%.

4. Conclusion

To conclude, using the conventional solid state reaction method, $Ca_{0.1}Na_{0.9}Ti_{0.1}Nb_{0.9}O_3$ was successfully prepared. The Rietveld analysis of X-ray diffraction, at room temperature, validated that there is a single phase tetragonal perovskite crystal structure with the *P4mm* space group. The vibrational Raman spectroscopy study at room temperature confirms our structural results. With broad and dispersive permittivity maxima based on empirical parameters (ΔT_m, ΔT_{cm}, and γ), the dielectric study of the composition offered typical characteristics of relaxor ferroelectrics. Furthermore, the relaxation behavior is triggered by monopolar based on the Vogel–Fulcher model. This behavior is similar to the thermally-activated process of the spin, wherein the freezing process is controlled by cluster-flipping and inter-cluster interaction mechanism. This composition can be of high significance. Indeed, industrially speaking, these applications require a relaxor character at room temperature with non-lead based ceramic.

Conflicts of interest

There are no conflicts to declare.

References

1 V. Westphal, W. Kleemann and M. D. Glinchuk, *Phys. Rev. Lett.*, 1992, **68**, 847–850.
2 S. B. Hemer, F. A. Selmi, V. V. Varadan and V. K. Varadan, *Mater. Lett.*, 1993, **5**, 317–324.
3 T. Hu, T. J. Price, D. M. Iddles, A. Uusimäki and H. Jantunen, *J. Eur. Ceram. Soc.*, 2005, **25**, 2531–2535.
4 S. Garcia, R. Font, J. Portelles, R. J. Q. U. I. Nones, J. Heiras and J. M. Siqueiros, *J. Electroceram.*, 2001, **3**, 101–108.
5 K.-T. Kim and C.-I. Kim, *Thin Solid Films*, 2005, **472**, 26–30.
6 S. Garcia, R. Font, J. Portelles, R. J. Q. U. I. Nones, J. Heiras and J. M. Siqueiros, *J. Electroceram.*, 2001, **3**, 101–108.
7 S.-G. Lee, R. G. Monteiro, R. S. Feigelson, H. S. Lee, M. Lee and S.-E. Park, *Appl. Phys. Lett.*, 1999, 1030–1032.
8 A. Lurio and G. Burns, *J. Appl. Phys.*, 1974, **45**, 1986–1992.
9 R. Brahem, H. Rahmouni, N. Farhat, J. Dhahri and K. Khiroun, *Ceram. Int.*, 2014, **40**, 9355–9360.
10 S. Chihaoui, L. Seveyrat, V. Perrin, I. Kallel, L. Lebrun and H. Khemakhem, *Ceram. Int.*, 2016, **123**, 305.

11 P. Sateesh, J. Omprakash, G. S. Kumar and G. Prasad, *J. Adv. Dielectr.*, 2015, **5**, 1550002–1550015.
12 H. Abdelkefi, H. Khemakhem, V. Gabriel and J. Claude, *J. Alloys Compd.*, 2005, **399**, 1–6.
13 L. P. Curecheriu, L. Mitoseriu and A. Ianculescu, *J. Alloys Compd.*, 2009, **482**, 1–4.
14 D. Kothari, V. Raghavendra Reddy, V. G. Sathe, A. Gupta, A. Banerjee and A. M. Awasthi, *Ceram. Int.*, 2015, **41**, 12958–12966.
15 X. Chen, Y. Li, F. Kong, L. Li, Q. Sun and F. Wang, *J. Alloys Compd.*, 2012, **541**, 505–509.
16 Y. J. Wong, J. Hassan and M. Hashim, *J. Alloys Compd.*, 2013, **571**, 138–144.
17 A. B. Hassen, F. I. H. Rhouma, J. Dhahri and N. Abdelmoula, *J. Alloys Compd.*, 2016, **663**, 436–443.
18 S. Sasaki, C. T. Prewitt and J. D. Bass, *Acta Crystallogr., Sect. C: Cryst. Struct. Commun.*, 1987, **43**, 1668–1674.
19 V. V. Lemanov, A. V. Sotnikov, E. P. Smirnova, M. Weihnacht and R. Kunze, *Solid State Commun.*, 1999, **110**, 611–614.
20 K. Konieczny, *Mater. Sci. Eng. B.*, 1999, **60**, 124–127.
21 S. Khemakhem, S. Yahyaoui, R. Ben Hassen, H. Khemakhem and A. Ben Salah, *Solid State Sci.*, 2003, **5**, 367–371.
22 M. Athee and A. W. Hewat, *Acta Crystallogr. A*, 1975, **31**, 846.
23 R. Von Der Mühll, A. Sadel and P. Hagenmuller, *J. Solid State Chem.*, 1984, **51**, 176.
24 S. Tripathi, A. Kumar, U. V. Waghmare and D. Pandey, *Phys. Rev. B*, 2010, **81**, 212101.
25 A. L. Goodwin, S. A. T. Redfern, M. T. Dove, D. A. Keen and M. G. Tucker, *Phys. Rev. B: Condens. Matter Mater. Phys.*, 2007, **76**, 1–4.
26 S. Tripathi, D. Pandey, S. K. Mishra and P. S. R. Krishna, *Phys. Rev. B: Condens. Matter Mater. Phys.*, 2008, **77**, 052104.
27 A. Simon, J. Ravez and M. Maglione, *Solid State Sci.*, 2005, **7**, 925–930.
28 J. B. Goodenough, *Phys. Rev.*, 1955, **100**, 564.
29 B. Y. R. D. Shannon, *Acta Crystallogr., Sect. A: Cryst. Phys., Diffr., Theor. Gen. Crystallogr.*, 1976, **32**, 751.
30 Z. Q. Li, E. Y. Jiang, S. W. Ren, D. L. Hou, P. Wu and H. L. Bai, *Phys. Status Solidi A*, 2003, **195**, 429–433.
31 V. Biju, N. Sugathan, V. Vrinda and S. L. Salini, Estimation of lattice strain in nanocrystalline silver from X-ray diffraction line broadening, *J. Mater. Sci.*, 2008, **43**, 1175–1179.
32 G. K. Williamson and W. H. Hall, *Acta Metall.*, 1953, **1**, 22.
33 K. S. Rao, B. Tilak, K. C. V. Rajulu, A. Swathi and H. Workineh, *J. Alloys Compd.*, 2011, **509**, 7121–7129.
34 I. P. Muthuselvam and R. N. Bhowmik, *J. Alloys Compd.*, 2012, **511**, 22–30.
35 Y. Chang, Z. Yang, M. Dong, Z. Liu and Z. Wang, *Mater. Res. Bull.*, 2009, **44**, 538–542.
36 S. D. Ross, *J. Phys. C: Solid State Phys.*, 1970, **3**, 1785–1786.
37 Y. D. Juang, M. L. Hu and W. S. Tse, *J. Appl. Phys.*, 1994, **76**, 3746.
38 L. Ben Abdessalem, M. Ben Abdessalem, A. Aydi and Z. Sassi, *J. Mater. Sci.: Mater. Electron.*, 2017, **28**, 14264–14270.
39 M. Zannen, A. Lahmar, M. Dietze, H. Khemakhem, A. Kabadou and M. Es-Souni, *Mater. Chem. Phys.*, 2012, **134**, 829–833.
40 S. Said, P. Marchet, T. Merle-Méjean and J.-P. Mercurio, *Mater. Lett.*, 2004, **58**, 1405–1409.
41 R. Selvamani, G. Singh, V. Sathe, V. S. Tiwari and P. K. Gupta, *J. Phys.: Condens. Matter*, 2011, **23**, 055901.
42 M. Zannen, H. Khemakhem, A. Kabadoub and M. Es-Souni, *J. Alloys Compd.*, 2013, **555**, 56–61.
43 L. Patricio, R. Hermans, N. Velasco, G. Tarrach, F. Schlaphof and C. Loppacher, *Surf. Sci.*, 2003, **532–535**, 493–500.
44 S. Aydi, A. Amouri, S. Chkoundali and A. Aydi, *Ceram. Int.*, 2017, **43**, 12179–12185.
45 J. Fuming, K. Seiji, Z. Changlei and F. Chude, *J. Appl. Phys.*, 2000, **88**, 3608–3612.
46 A. Aydi, A. Simon, D. Michau, R. V. Der Muhll, N. Abdelmoula and H. Khemakhem, *J. Optoelectron. Adv. Mater.*, 2012, **14**, 251–256.
47 D. M. Fanning, I. K. Robinson, S. T. Jung, E. V. Colla, D. D. Viehland and D. A. Payne, *J. Appl. Phys.*, 2000, **87**, 840–848.
48 A. Kharouf, A. Aydi and K. Khirouni, *J. Alloys Compd.*, 2019, **775**, 81–89.
49 X. Dai, A. DiGiovanni and D. Viehland, *J. Appl. Phys.*, 1993, **74**, 3399–3405.
50 F. Boujelben, F. Bahri, C. Boudaya, A. Maalej, H. Khemakhem, A. Simon and M. Maglione, *J. Alloys Compd.*, 2009, **481**, 559–562.
51 A. Aydi, A. Simon, D. Michau, R. Von Der Mühll, N. Abdelmoula and H. Khemakhem, *J. Alloys Compd.*, 2011, **509**, 7773–7777.
52 C. Chaker, Y. Gagou, N. Abdelmoula, J.-L. Dellis, C. Masquelier, H. Khemakhem and M. El Marssi, *J. Appl. Phys.*, 2012, **111**, 044101.
53 I. Kallel, Z. Abdelkafi, N. Abdelmoula, A. Simon and H. Khemakhem, *Bull. Mater. Sci.*, 2013, **36**, 893–898.
54 S. Q. Jan, M. Usman, M. N. Ul-Haq and A. Mumtaz, *J. Alloys Compd.*, 2018, **735**, 1893–1900.
55 Z. Raddaoui, S. El Kossi, J. Dhahri, N. Abdelmoula and K. Taibi, *RSC Adv.*, 2019, **9**, 2412.
56 T. Badapanda, S. Rout, L. Cavalcante, J. Sczancoski, S. Panigrahi, E. Longo and M. S. Li, *J. Phys. D: Appl. Phys.*, 2009, **42**, 175414.
57 L. E. Cross, *Ferroelectrics*, 1994, **151**, 305–320.
58 A. Aydi, S. Chkoundali, H. Khemakhem, A. Simon and R. Von der Mühl, *J. Alloys Compd.*, 2008, **465**, 222–226.
59 G. A. Smolenskii, *J. Phys. Soc. Jpn.*, 1970, **28**(Suppl 2), 26.
60 V. V. Kirillov and V. A. Isupov, *Ferroelectrics*, 1973, **5**, 3–9.
61 F. Bourguiba, Ah. Dhahri, T. Tahri, J. Dhahri, N. Abdelmoula, K. Taibi and E.-K. Hlil, *J. Alloys Compd.*, 2016, **675**, 174–182.
62 H. T. Martirena and J. C. Burfoot, *Ferroelectrics*, 1974, **7**, 151–152.
63 H. Vogel, *Phys. Z.*, 1921, **22**, 645–667.
64 G. Fulcher, Analysis of recent measurements of the viscosity of glasses, *J. Am. Ceram. Soc.*, 1925, **8**, 339–355.
65 D. Viehland, S. Jang, L. E. Cross and M. Wittig, *J. Appl. Phys.*, 1990, **68**, 2916–2921.
66 H. Ghoudi, S. Chkoundali, A. Aydi and K. Khirouni, *Appl. Phys. A*, 2017, **123**, 703.